JACS
JOURNAL OF THE AMERICAN CHEMICAL SOCIETY
Article
pubs.acs.org/JACS

Cooperativity and Dynamics Increase the Performance of NiFe Dry Reforming Catalysts

Sung Min Kim,[†] Paula Macarena Abdala,[†] Tigran Margossian,[‡] Davood Hosseini,[†] Lucas Foppa,[‡] Andac Armutlulu,[†] Wouter van Beek,[§] Aleix Comas-Vives,[‡] Christophe Copéret,[‡] and Christoph Müller*[,†]

[†]Laboratory of Energy Science and Engineering, Department of Mechanical and Process Engineering, ETH Zurich, Leonhardstrasse 21, Zurich 8092, Switzerland

[‡]Department of Chemistry and Applied Sciences, ETH Zurich, Vladimir Prelog Weg 1-5, Zurich 8093, Switzerland

[§]Swiss-Norwegian Beamlines, European Synchrotron Radiation Facility (ESRF), BP 220, Grenoble 38043, France

Supporting Information

ABSTRACT: The dry reforming of methane (DRM), i.e., the reaction of methane and CO_2 to form a synthesis gas, converts two major greenhouse gases into a useful chemical feedstock. In this work, we probe the effect and role of Fe in bimetallic NiFe dry reforming catalysts. To this end, monometallic Ni, Fe, and bimetallic Ni-Fe catalysts supported on a $Mg_xAl_yO_z$ matrix derived via a hydrotalcite-like precursor were synthesized. Importantly, the textural features of the catalysts, i.e., the specific surface area (172−178 m^2/g_{cat}), pore volume (0.51−0.66 cm^3/g_{cat}), and particle size (5.4−5.8 nm) were kept constant. Bimetallic, Ni_4Fe_1 with Ni/(Ni + Fe) = 0.8, showed the highest activity and stability, whereas rapid deactivation and a low catalytic activity were observed for monometallic Ni and Fe catalysts, respectively. XRD, Raman, TPO, and TEM analysis confirmed that the deactivation of monometallic Ni catalysts was in large due to the formation of graphitic carbon. The promoting effect of Fe in bimetallic Ni-Fe was elucidated by combining operando XRD and XAS analyses and energy-dispersive X-ray spectroscopy complemented with density functional theory calculations. Under dry reforming conditions, Fe is oxidized partially to FeO leading to a partial dealloying and formation of a Ni-richer NiFe alloy. Fe migrates leading to the formation of FeO preferentially at the surface. Experiments in an inert helium atmosphere confirm that FeO reacts via a redox mechanism with carbon deposits forming CO, whereby the reduced Fe restores the original Ni-Fe alloy. Owing to the high activity of the material and the absence of any XRD signature of FeO, it is very likely that FeO is formed as small domains of a few atom layer thickness covering a fraction of the surface of the Ni-rich particles, ensuring a close proximity of the carbon removal (FeO) and methane activation (Ni) sites.

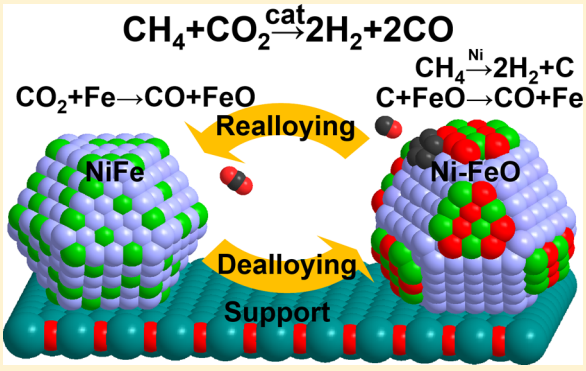

1. INTRODUCTION

The dry reforming of methane (DRM), i.e., the reaction of methane and CO_2 forming synthesis gas with a H_2:CO molar ratio close to unity, converts two major greenhouse gases into a useful chemical feedstock. Several transition metals including Ru, Rh, Pt, Co, and Ni are active in the DRM,[1−5] but Ni-based catalysts are preferred because they combine good activity and low costs (compared to noble metals).[6] However, Ni-based catalysts suffer from rapid deactivation, due to metal oxidation[7] and particle sintering[8,9] as well as coke formation.[10,11] Several strategies, such as control of the Ni particle size, have been shown to minimize coke formation.[12] A further strategy has utilized basic supports[13−18] or the doping of the catalyst with alkali metals[19−28] to increase surface basicity,[13−18] hence facilitating the activation of CO_2 to gasify carbon. More recently, the addition of secondary metals to Ni has been proposed as an effective approach to improve its catalytic stability. The improved activity and stability of Ni alloys containing noble (Pt, Rh, Pd, and Ru)[21−24] or non-noble (e.g., Fe, Cu, Mn, and Co) metals[25−29] have been attributed largely to the reduced formation of coke, albeit the underlying mechanism has not been elucidated in detail yet.[30−33] From an economic point of view, the use of Fe would be highly desirable due to its low price (approximately 250 times lower than that of Ni or Co).[34−36] Nevertheless, currently there are contradicting reports on whether the addition of Fe to Ni catalysts has indeed a positive effect on the catalyst's activity or not.[26,37−39] In addition, also the mechanism behind the altered catalytic behavior of these bimetallic systems is unclear. For example, the study of Zhang et al.[22] that assessed different Ni-M alloys (M = Co, Cu, Mn, and Fe) supported on $MgAl_2O_4$ found that only

Received: November 4, 2016
Published: January 9, 2017

ACS Publications © 2017 American Chemical Society

DOI: 10.1021/jacs.6b11487
J. Am. Chem. Soc. 2017, 139, 1937−1949

Co was promoting the activity of Ni, while Ni-Fe catalysts showed a high rate of coke formation and a low activity for DRM when compared to other Ni-M alloys.[26] However, further studies observed that the Fe/Ni ratio critically determines whether Fe has a promoting or suppressing effect on the catalytic activity.[37−39] Moreover, it is conceivable that also the type of support can affect whether the addition of Fe increases or decreases the catalytic performance. For example, the doping of silica with La^{3+} ions was found to improve the activity and stability of Ni DRM catalysts.[40] This was attributed to an increased CO_2 adsorption and hydrogen adsorption strength with increasing La doping, owing to an electronic interaction between Ni and La silicates. Furthermore, in the case of bimetallic catalysts, the presence of a second metal (e.g., Co) can affect the rate of formation of $La_2O_2CO_3$, which, in turn, has been reported to affect positively the rate of removal of the carbon deposited.[41] On the other hand, the addition of Fe (Ni-Fe@La_2O_3) was found to reduce significantly the activity of the catalyst when compared to Ni@La_2O_3 or Ni-Co@La_2O_3, owing to the encapsulation of active Ni particles by a $LaFeO_3$ phase that was formed under DRM conditions.[41] Several studies have indicated that the formation of a Ni-Fe alloy plays an important role for the catalyst's stability under steam or dry reforming conditions,[41−44] however, currently there is no agreement on a mechanism that would explain the improved coke resistance of Ni-Fe alloys. This is largely due to the lack of a detailed understanding of the structure of Ni-Fe catalysts under practically relevant reaction conditions. For example, one study attributed the low rate of coke deposition observed on Ni-Fe/Mg(Al)O under steam reforming conditions to the homogeneous distribution (and proximity) of Fe and Ni atoms in a NiFe alloy, whereby surface oxygen of Fe-activated steam gasifies the coke formed on Ni sites.[39,42] An alternative explanation proposed the inhibition of carbon formation on a NiFe alloy by a "dilution effect" of the Ni active sites by Fe, thus reducing the effective size of "Ni clusters".[45] Recently, *in situ* XRD experiments on Ni-Fe/$MgAl_2O_4$ in CH_4/CO_2 atmospheres with varying CH_4:CO_2 ratios have indicated that under DRM conditions, dealloying may occur. However, the formation of FeO was only observed at very high partial pressures of CO_2 (CH_4:CO_2 = 1:6). Hence, it is currently unclear whether FeO_x is formed also under realistic dry reforming conditions, i.e., CH_4:CO_2 ∼ 1:1 (650 °C). Overall, the role of Fe in Ni-based DRM catalysts remains unknown.

This work has therefore aimed at obtaining an understanding at the atomic level on how the addition of Fe affects the performance, i.e., the activity and stability, of Ni-Fe-based DRM catalysts. Since several material properties may affect the activity and stability of Ni-based catalysts, e.g., particle size or porous structure, great care was taken to prepare supported metallic and bimetallic catalyst systems with identical textural properties, varying only the ratio of Fe to Ni. To this end, Ni-Fe-based catalysts were prepared from a hydrotalcite-structured precursor, allowing to obtain, after calcination and reduction, Ni-Fe nanoparticles of constant particle size in a Mg(Al)O matrix.[46,47] Applying advanced synchrotron X-ray-based characterization techniques under operando conditions, we were able to (i) correlate the Fe/Ni ratio with the activity and stability of the catalysts, (ii) determine the structure of the catalysts, i.e., the stability of the alloy, the oxidation state of the metals, and the metals distribution under DRM conditions; and (iii) understand the mechanism through which Fe affects the coke resistance of Ni-based catalysts.

2. EXPERIMENTAL SECTION

2.1. Catalysts Preparation. Ni-, Fe-, and Ni-Fe-based (Ni_4Fe_1, Ni_3Fe_1, Ni_1Fe_1, and Ni_1Fe_3) catalysts derived through a hydrotalcite-type precursor were prepared via coprecipitation. Specifically, a 1.0 M nitrate solution containing adjusted amounts of $Ni(NO_3)_2{\cdot}6H_2O$, $Mg(NO_3)_2{\cdot}6H_2O$, $Fe(NO_3)_3{\cdot}9H_2O$, and $Al(NO_3)_3{\cdot}9H_2O$ was added dropwise to a 0.2 M Na_2CO_3 solution. A pH value of 10 ± 0.5 was maintained by adding appropriate amounts of 2.0 M NaOH (or 1.0 M nitric acid). The weight fraction of Ni + Fe was 10 wt %, and the molar ratio of divalent metals (Ni^{2+} and Mg^{2+}) to trivalent metals (Fe^{3+} and Al^{3+}) was fixed to 2.0. The mixture obtained was aged at room temperature for 24 h. The resulting precipitates were filtered and washed with deionized water (reverse osmosis, 15 MΩ·cm) until the electrical conductivity of the filtrate was <100 μS/cm. The precipitates were dried at 100 °C overnight and calcined at 800 °C for 5 h using a heating rate of 5 °C/min. The calcined catalysts were crushed and sieved to a particle size range 100−300 μm. The as-synthesized catalysts are labeled as Ni-MA and Fe-MA for the monometallic Ni and Fe catalysts and Ni_xFe_y-MA (x and y give the molar ratio of Ni to Fe = x:y) for the bimetallic catalysts.

2.2. Catalysts Characterization. Elemental analysis of the calcined materials was performed on a ICP-OES (Varian 720-ES).

Nitrogen physisorption was performed in a NOVA 4000e (Quantachrome) instrument at −196 °C. Prior to the experiment, the samples were degassed at 300 °C for 3 h. The specific surface area and pore volume were calculated using the Brunauer−Emmett−Teller (BET)[48] and Barrett−Joyner−Halenda (BJH) models,[49] respectively.

Temperature-programmed reduction (TPR), oxidation (TPO), and carbon deposition experiments were performed in a thermogravimetric analyzer (TGA, Mettler Toledo TGA/DSC). The following procedure was used for TPR: A small amount of catalyst (40−50 mg) was placed in an alumina crucible and heated to 1000 °C (10 °C/min ramp) under a flow (50 mL/min) of 10 vol % of H_2 in N_2. The mole fraction of H_2 in the off-gas was measured using a thermal conductivity detector (ABB Caldos27). TPO experiments were performed to determine the coking characteristics of the materials. Using a TGA, the weight loss of the reacted material (10−15 mg) during oxidation (50 mL/min air) was recorded continuously. The carbon deposition rate and the total amount of carbon deposited were determined by recording continuously the weight increase of a reduced catalyst that was exposed at 650 °C to an atmosphere containing 5 vol % CH_4, 5 vol % CO_2, and 90 vol % N_2 (flow rate 100 mL/min).

Hydrogen chemisorption was conducted in a BELCAT-M (equipped with a thermal conductivity detector). In a typical experiment, 50 mg of the calcined catalyst was reduced in a quartz reactor at 800 °C for 2 h using 5 vol % H_2 in Ar. Subsequently the sample was purged with Ar at 800 °C for 30 min and cooled down to 50 °C. The quantity of chemisorbed hydrogen was determined at 30 °C by periodically injecting pulses of 5 vol % H_2 in Ar over the reduced catalyst. The stoichiometry factor between dissociated H_2 and active metal (Ni, Fe, and Ni-Fe alloy) was assumed to be 1.0 (H/M).[50−52]

The crystalline phases in the catalysts were determined by powder X-ray diffraction (XRD, Bruker AXS D8 Advance). The X-ray diffractometer was equipped with a Lynxeye super speed detector using Cu K_α radiation (40 mA and 40 kV). The scans were collected in the 2θ range 5−90° (step size: 0.05° and time per step 0.8 s).

The morphology, particle size, and particle composition of the reduced and reacted catalysts were analyzed by TEM (Philips CM 12, 100 kV), HR-TEM (FEI F30 FEG, 300 kV), and STEM (Hitachi HD-2700).

Coke deposition was characterized further by Raman spectroscopy (Thermo Scientific). The Raman spectra were acquired in the range 500−3500 cm^{-1} using a laser with a wavelength of 514.5 nm. The spectral resolution employed was 4 cm^{-1}.

2.3. DRM Catalytic Tests. The DRM reaction was carried out in a fixed-bed quartz reactor (400 mm length, 12.6 mm internal diameter). In a typical experiment, 20 mg of the calcined catalyst was used. Prior to the activity tests, the catalyst was reduced in 10 vol % H_2/N_2 at 800

DOI: 10.1021/jacs.6b11487
J. Am. Chem. Soc. 2017, 139, 1937−1949

Table 1. Physicochemical Properties of the Prepared Catalysts

	ICP-AES[a]			N_2 physisorption[b]				H_2 consumption[c]		
catalyst	Ni [%]	Fe [%]	M^{2+}/M^{3+}	S_{BET} [m^2/g]	V_p [cc/g]	R_p [nm]	H_2 chemisorption [$\mu mol/g_{cat}$]	$mmol_{H_2}/g_{cat}$	$mol_{H_2}/mol_{Ni,\ Fe,\ or\ NiFe}$	particle size[d] [nm]
Ni-MA	10.1	0.0	1.98	178	0.51	2.6	98	1.67	0.97	5.4
Ni_4Fe_1-MA	8.8	2.1	1.75	174	0.54	2.5	79	1.85	0.99	5.4
Ni_3Fe_1-MA	7.7	2.3	1.96	177	0.61	3.0	61	1.92	1.11	5.5
Ni_1Fe_1-MA	5.2	4.8	1.98	175	0.61	3.0	30	2.03	1.16	5.6
Ni_1Fe_3-MA	2.7	7.2	1.87	172	0.66	3.1	16	2.11	1.20	5.6
Fe-MA	0.0	9.7	1.91	175	0.61	2.8	1	2.37	1.37	5.8

[a]The weight percent of Ni and Fe in the materials is reported in the Ni and Fe columns, and the molar ratio between divalent metals (Ni + Mg) and trivalent metals (Fe + Al) is given in the M^{2+}/M^{3+} column. [b]The specific surface area, pore volume, and pore radius were calculated using BET and BJH models. [c]The quantity of H_2 consumed was divided by the quantity of Ni, Fe, or NiFe determined by ICP-AES. [d]Average monometallic or bimetallic particle size (catalysts reduced at 800 °C for 2 h) as determined by TEM.

°C for 2 h. Subsequently, the bed was cooled down to 650 °C to perform the DRM activity tests. The total flow rate of the feed gas was 100 mL/min (270,000 $mL \cdot g_{cat}^{-1} \cdot h^{-1}$ of GHSV; composition: 45% CH_4, 45% CO_2, and 10% N_2). The composition of the off-gas was analyzed via a micro-GC (thermal conductivity detector (TCD); molecular sieve 5A; and U-plot column cartridges).

2.4. XAS and Synchrotron XRD Experiments. Combined X-ray absorption spectroscopy (XAS) and powder XRD experiments were performed at the Swiss-Norwegian Beamlines (SNBL, BM01B) at the European Synchrotron Radiation Facility (ESRF). XAS spectra were collected at the Ni and Fe K-edges using a double-crystal Si (111) monochromator (continuous scanning in transmission mode). XRD data were collected with a 2D DEXELA detector using a Si (111) channel-cut monochromator, set at a wavelength of 0.5060 Å.[53] Alternate XAS-XRD data were collected (Ni-MA and Ni_4Fe_1-MA) during temperature-programmed reduction (room temperature to 850 °C) and under DRM conditions (650 °C for 5 h of operation) using a capillary reactor cell.[54] After the first reduction step, the samples were cooled down to 50 °C (in H_2) and XRD + EXAFS data were recorded (temperature and gas composition as a function of time are shown in Figure S1). Pellets made of NiO, Ni-Fe alloys, Ni_3C, FeO, Fe_3O_4, Fe_2O_3, (MgFe)O and (MgNi)O with a periclase structure, $MgNi_2O_4$, and $MgFe_2O_4$ as well as Fe and Ni foils were used as references. The reference materials (MgFe)O, (MgNi)O, $MgNi_2O_4$, and $MgFe_2O_4$ were synthesized according to previously reported protocols.[55,56] XAS data reduction and analysis were carried out using the Athena software.[57] EXAFS fittings were performed on the data collected at room temperature using the Artemis software.[57]

2.5. Thin-Film Preparation and Characterization. Thin films of Al_2O_3 and Ni-Fe were deposited onto 3-in., p-type Si(100) wafers with a total thickness of 381 μm (Si-Mat Silicon Materials, Germany) using a magnetron sputtering system (PVD Products Inc., USA). The base pressure of the chamber was 3.1×10^{-7} Torr. The deposition of the Al_2O_3 film was performed via reactive sputtering from an Al target at 5 mTorr, 300 W, 50 sccm Ar flow, and 5 sccm O_2 flow. Ni-Fe films were deposited by cosputtering from their respective targets simultaneously at 3 mTorr, 20 sccm Ar flow. The deposition power of the respective Ni and Fe targets was varied from 100 W to 250 W to adjust the Ni:Fe ratio. During the cosputtering process, Ni and Fe targets were aligned in a confocal manner opposite to each other, where the target surfaces were tilted by 35° with respect to the substrate surface. To achieve a uniform film deposition, the substrate was rotated at 30 rpm throughout the sputtering process.

The thin films were exposed to reducing (800 °C in a flow of 10 vol % H_2 in N_2) and DRM conditions (800 °C in a flow of 10 vol % CO_2, 10 vol % CH_4 balance N_2) in a thermogravimetric analyzer (TGA, Mettler Toledo TGA/DSC). They were characterized using a focused ion beam scanning electron microscopy (FIB-SEM, NVision 40, Zeiss, Germany) and energy dispersive X-ray spectroscopy (EDX).

2.6. Theoretical Calculations. The periodic density functional theory (DFT) calculations were carried out with the Vienna Ab Initio Simulation Package (VASP) code[58−60] and the projector augmented wave (PAW) method,[61] for which interactions between valence electrons and ion cores are described by pseudopotentials, and the electronic wave functions are expanded in terms of a discrete plane wave basis set. A plane wave energy cutoff of 400 eV was used for all calculations. Electron exchange and correlation were treated with the generalized gradient approximation (GGA) by means of the Perdew−Wang (PW91) functional.[62] Brillouin zone sampling was performed using Monkhorst−Pack grids[63] ($3 \times 3 \times 1$ and $5 \times 5 \times 1$ for Ni and Ni_3Fe_1 surfaces, respectively). Electronic occupancies were determined according to a Methfessel−Paxton scheme with an energy smearing of 0.2 eV. Spin-polarized effects were considered in all calculations. Self-consistent field (SCF) calculations of the electronic structure were considered converged when the electronic energy change between two steps was below 10^{-6}. All geometries were optimized using an energy-based conjugate gradient algorithm until the forces acting on each atom were converged below 0.01 eV/Å. The energy of isolated molecules was determined by a Γ-point calculation placing each species in a box with dimensions $15 \times 15 \times 15$ Å. The climbing image nudge elastic band (CI-NEB) method[64] with eight intermediate images was used to locate transition states (TS). It was further confirmed that TS structures actually corresponded to saddle points by a frequency analysis. Normal vibration modes of adsorbed species were calculated by diagonalization of the Hessian matrix, obtained using a central finite difference approximation with displacements of 0.015 Å in the direction of each Cartesian coordinate. All metal atoms were kept fixed during the frequency calculations of adsorbed species. Reaction (electronic) energy diagrams and energy barriers were constructed assuming that there is an infinite separation between co-adsorbed species, i.e., the energy of co-adsorbed species is equal to the sum of the individual adsorption energies. All the reported energy values correspond to electronic energies.

In order to model the catalysts, (111) surfaces for Ni and Ni_3Fe_1 were constructed. Ni (111) and Ni_3Fe_1 (111) surface slabs were taken with dimensions equal to 3×3 and 4×4, respectively, using four-layer slabs with a vacuum separation of 15 Å in the direction perpendicular to the surface, as shown in Figure S2. Metal atoms from the bottom layer were kept fixed in their crystal lattice positions during all optimizations. For the calculations involving oxygen adsorption on Ni_3Fe_1 (111) surfaces, a smaller 3×3 slab with 5 layers was used instead using a $10 \times 10 \times 10$ k-point grid.

3. RESULTS AND DISCUSSION

3.1. Structure, Morphology and Physicochemical Properties of the Calcined Catalysts. XRD data of the dried materials shows a hydrotalcite-like structure, which after calcination at 800 °C transformed into a periclase [Mg(Ni,Fe)-O]-type structure with a minor quantity of a spinel [Mg-$(Al,Fe)_2O_4$]-type phase (Figure S3). In the diffraction data of the calcined materials, neither NiO nor Fe_2O_3 phases were detected. The (200) reflection of the periclase structure is observed at *d*-spacings in the range 2.0928−2.1021 Å

DOI: 10.1021/jacs.6b11487
J. Am. Chem. Soc. 2017, 139, 1937−1949

(depending on the Ni/Fe ratio). These values are smaller than the values for MgO (d = 2.1045 Å) due to the incorporation of cations smaller than Mg^{2+} (0.69 Å), e.g., Ni^{2+} (0.62 Å), Fe^{3+} (0.64 Å), and Al^{3+} (0.54 Å) into the periclase structure (Figure S4). Further structural information on the local environment around Ni and Fe was obtained by XAS analysis at the Ni and Fe K-edges. For data analysis, the following reference materials were also measured: ternary oxides of Ni and Fe exhibiting pure spinel and periclase-type structures (i.e., Mg(Ni)O and Mg(Fe)O periclases; $MgFe_2O_4$ and $MgNi_2O_4$ spinels); and the corresponding binary oxides (Fe_2O_3, Fe_3O_4, FeO and NiO). As each of these references have well distinguishable features in their XANES signature, we were able to determine the environment around Ni and Fe atoms by linear combination fitting (LCF) analysis. Using Fe K-edge XANES data, LCF shows that Fe is present in both periclase and spinel phases. The distribution of Fe^{3+} was determined as 83% in the periclase and 17% in the spinel phase in all Ni_xFe_y-MA catalysts and as 70% in the periclase and 30% in the spinel phase for Fe-MA. On the other hand, the Ni K-edge data of the calcined material are identical to the Mg(Ni)O periclase standard, and linear combination yielded 100% of this standard. This allows us to conclude that all Ni is in a periclase structure. *In situ* synchrotron XRD + XAS studies discussed in the following section confirmed these findings and gave further insight in the formation of metallic particles from the mixed oxides under reductive conditions.

The elemental composition and the results of the N_2 physisorption characterization of the catalysts are summarized in Table 1. The weight fraction of Ni and Fe in the calcined catalysts, as determined by ICP-AES, and the molar ratio of the divalent (Ni^{2+} and Mg^{2+}) metals are in good agreement with the nominal values of the synthesis protocols. N_2 physisorption experiments confirmed that the textural properties of the different catalysts were very similar, i.e., the specific surface areas, pore volumes, and pore diameters were in the range 172−175 m^2/g_{cat}, 0.25−3.0 cc/g_{cat}, and 2.5−3.0 nm, respectively. All calcined materials showed a type IV isotherm with a hysteresis loop between p/p_0 = 0.6−1.0 (Figure S5).

3.2. Formation of Bimetallic Nanoparticles upon Reduction. Before reaction, the calcined catalysts were pretreated in H_2 at 800 °C to form metallic and bimetallic nanoparticles. The reduced materials (i.e., before reaction) were characterized by XRD, TEM, and H_2-chemisorption analysis. To obtain insight into the reduction process of the Mg(Al,Ni,Fe)O solid solutions, H_2-TPR (TGA) and *in situ* XAS-XRD experiments were performed.

The diffractograms of the reduced catalysts with Ni/(Ni + Fe) ratios in the range 0.5−1.0 exhibit a fcc crystal structure ($Fm\bar{3}m$ space group). Conversely, α-Fe and Ni-Fe alloys with a bcc crystal structure ($Im\bar{3}m$ space group) were detected for Ni/(Ni + Fe) ratios in the range 0−0.25 (Figure S6a). In excellent agreement with Vegard's law (Figure 1), a linear relationship between the cell parameter of fcc Ni-Fe and the Ni/(Ni + Fe) ratio (range 0.5−1.0) was obtained.[65,66] TEM and STEM EDX (Figure S6b and Figure 1b) confirmed that the reduced metal particles (Ni, Fe, and Ni-Fe alloys) were well dispersed and that the particle sizes were in the range of 5.4−5.8 nm, independent of the ratio of Fe/(Ni + Fe). A constant particle size is critical to probe exclusively the effect of the Ni/(Ni + Fe) ratio on the catalytic activity of the material. The Ni to Fe ratio in the reduced metal particles, as determined by STEM EDX (Figure 1b), is on average 4.1 ± 0.2 and 3.1 ± 0.3 for, respectively,

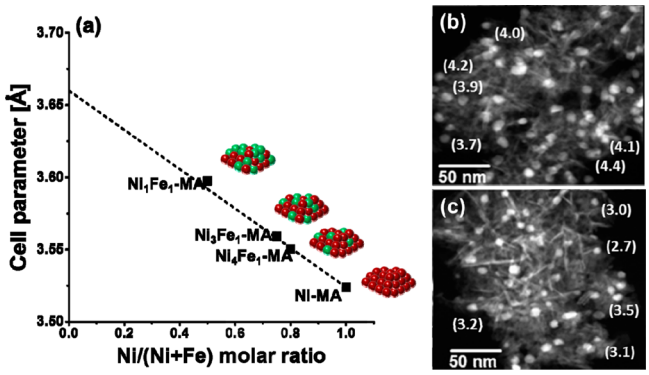

Figure 1. (a) The fcc Ni-Fe cell parameter obtained from the (200) Bragg reflection of the XRD data of the reduced catalysts as a function of the molar ratio Ni/(Ni + Fe). The dashed line gives the theoretical cell parameter according to Vegard's law.[65,66] STEM images combined with EDX analysis of reduced (b) Ni_4Fe_1-MA and (c) Ni_3Fe_1-MA. The Ni/Fe ratio of selected particles, as determined by EDX analysis, is denoted in parentheses.

Ni_4Fe_1-MA and Ni_3Fe_1-MA, confirming further the formation of Ni-Fe alloys upon reduction.

H_2 chemisorption experiments revealed that the quantity of chemisorbed H_2 (Table 1) decreased with an increasing Fe/(Ni + Fe) ratio, yielding only 1 $\mu mol/g_{cat}$ for Fe-MA. These results are in agreement with previous studies and suggest that H_2 is chemisorbed only on Ni under the explored conditions.[39,67,68] This point will be discussed further in the context of catalytic activity (Section 3.3).

The H_2-TPR profiles of the calcined materials and the corresponding quantities of H_2 consumed are reported in Figure S7 and Table 1. For Ni-MA, the single peak located at 783 °C is attributed to the reduction of Ni^{2+} to metallic Ni, while for Ni_4Fe_1-MA and Ni_3Fe_1-MA, the peaks are shifted to higher temperatures. In the case of Fe-MA, three reduction peaks located at 582, 768, and 942 °C are ascribed to the sequential reduction of Fe_2O_3 to metallic Fe via Fe_3O_4, i.e., an equimolar mixture of Fe^{2+} and Fe^{3+} and FeO intermediates.[69,70] Similarly, for low-Ni content materials, i.e., Ni_1Fe_1-MA and Ni_1Fe_3-MA, peaks due to the reduction of Ni and Fe were identified.

To resolve temporally the formation of metallic and bimetallic nanoparticles, combined *in situ* XRD-XAS experiments at the Ni and Fe K-edges were performed for Ni-MA and Ni_4Fe_1-MA (Figure 2 and Figure S8). Ni K-edge XANES and XRD show the formation of Ni or a Ni-Fe alloy in the temperature range 800−850 °C. In the case of Ni_4Fe_1-MA, Fe K-edge XANES (Figure 2e, and LCF analysis in Figure S8h) reveals that Fe_2O_3 was reduced sequentially through Fe_3O_4 and FeO intermediates to finally metallic Fe. However, the absence of reflections from Fe_3O_4 or FeO phases in the XRD data suggests that the partially reduced Fe species remained in the periclase/spinel phases or formed only very small domains of FeO_x. When compared to nickel oxide, iron oxides required higher temperatures and longer reduction times for full reduction.[37,47] The formation of a NiFe alloy was observed in both XAS and XRD data. Figure S9 plots Ni and Fe K-edge XANES spectra of reduced Ni-MA and Ni_4Fe_1-MA. Good agreement with the metallic and bimetallic references is observed. The formation of a NiFe alloy is evidenced by XRD through a shift in the (200) peak position of fcc NiFe when compared to the monometallic reference (Figure 1).

DOI: 10.1021/jacs.6b11487
J. Am. Chem. Soc. 2017, 139, 1937−1949

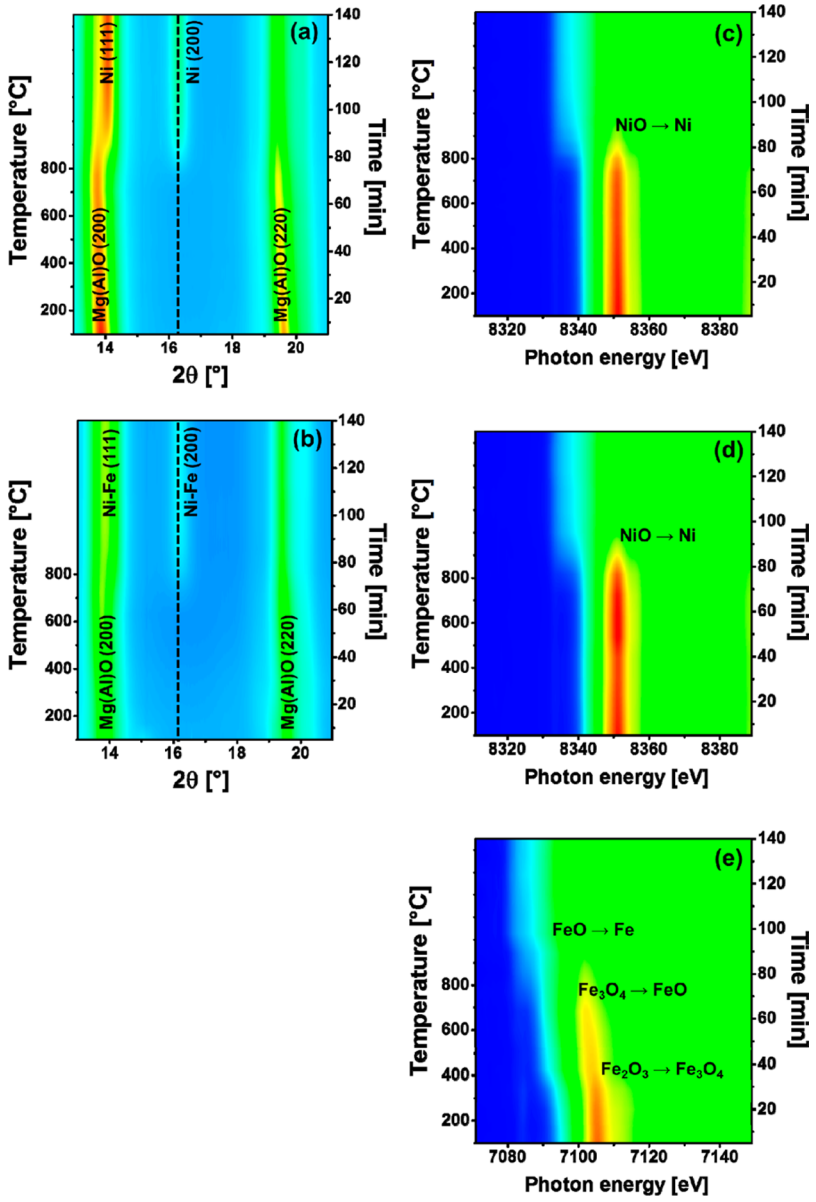

Figure 2. Contour plots of the acquired *in situ* XRD data (λ = 0.5060 Å): (a) Ni-MA and (b) Ni_4Fe_1-MA during reduction as a function of time and temperature (heating rate 5 °C/min, up to 850 °C), followed by isothermal reduction. The most prominent XRD reflections are labeled. The dashed line indicates the position of Ni (200). The corresponding XANES data at the Ni K-edge: (c) Ni-MA and (d) Ni_4Fe_1-MA and at the Fe K-edge: (e) Ni_4Fe_1-MA.

EXAFS analysis of the data collected on the reduced samples (acquired in the *in situ* setup after cooling down to 50 °C in He) is in line with the formation of a NiFe alloy. The normalized EXAFS data in *k*-space and the corresponding Fourier transforms in *R* space at both Ni and Fe K-edges are presented in Figure S10. At the Ni-edge, the EXAFS oscillations of the monometallic system (Ni-MA) agree with the signatures of the Ni foil, while for bimetallic Ni_4Fe_1-MA, the oscillations are shifted to slightly higher *k* values (Figure S10a). A comparison between the Fe K edge data (Figure S10c and S10d) of Ni_4Fe_1-MA and the Fe foil (bcc) and bulk Ni-Fe alloy (fcc) references confirms the alloying of Fe in a fcc structure in the reduced bimetallic material (in agreement with the XANES data). The lower amplitude of the oscillations in the catalyst samples when compared to the bulk references (at both edges) is due to finite size effects in the nanoparticles.

The fitting results of the Ni and Fe K-edge EXAFS data of the as-reduced Ni-MA and Ni_4Fe_1-MA are listed in Tables S1 and S2 and shown in Figure S17. EXAFS data analysis was carried out by fitting simultaneously the Ni and Fe K-edge data, while applying physically motivated constraints as outlined in the SI.[71] The good quality of the fit and the obtaining of physically meaningful values for the best-fit results confirm that both Ni and Fe are in an fcc environment in the reduced bimetallic materials. In addition, the results are consistent with the formation of an fcc NiFe alloy with a high degree of atomic mixing (more details are provided in the SI). This is in good agreement with STEM-EDX. However, the somewhat lower total coordination number of Fe-metal (7.7 ± 0.7) compared to Ni-metal (9.1 ± 1) indicates a slight preference of Fe to be located on the surface of the alloy nanoparticle.

3.3. Effect of Fe on the catalytic Performance. The activity of the catalysts for the DRM (at 650 °C) quantified as

DOI: 10.1021/jacs.6b11487
J. Am. Chem. Soc. 2017, 139, 1937−1949

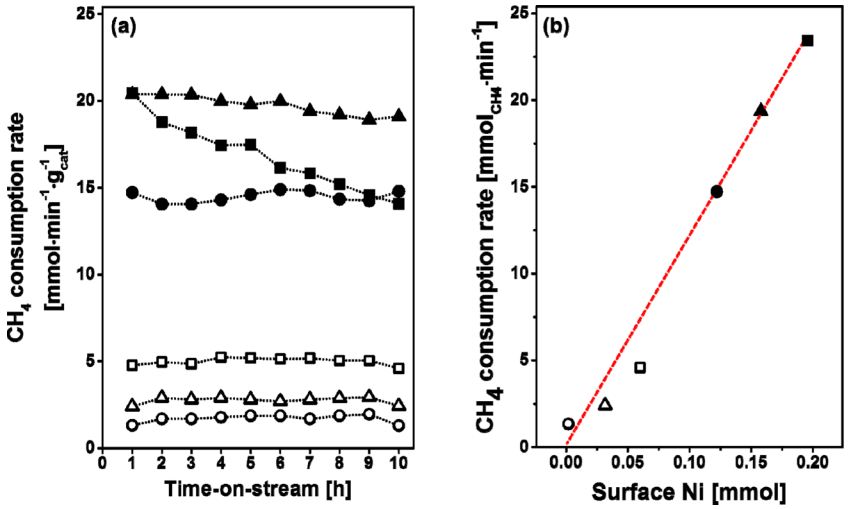

Figure 3. (a) Rate of methane consumption as a function of TOS and (b) rate of methane consumption (after 1 h TOS) as a function of the quantity of surface Ni: (■) Ni-MA, (▲) Ni_4Fe_1-MA, (●) Ni_3Fe_1-MA, (□) Ni_1Fe_1-MA, (△) Ni_1Fe_3-MA and (○) Fe-MA.

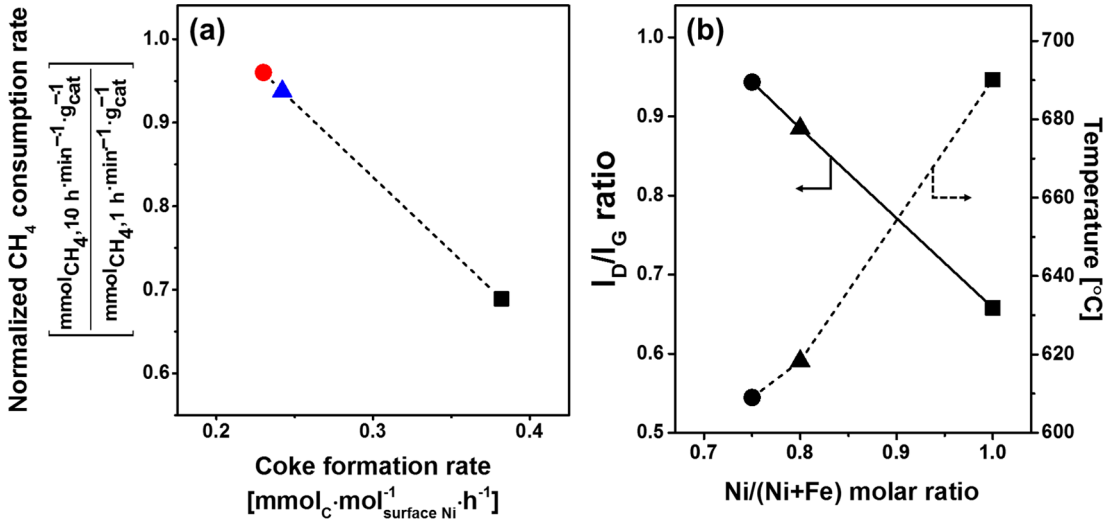

Figure 4. (a) Rate of methane consumption (after 10 h of TOS) normalized by the initial rate of methane consumption (1 h of TOS), as a function of the rate of carbon formation. (b) Ratio of D- and G-band intensities in the spent catalysts (I_D/I_G) and the temperature for coke removal as a function of the Ni/(Ni + Fe) molar ratio.

the rate of methane consumption, normalized by the mass of the catalyst, is plotted in Figure 3a. For Fe-MA, the rate of CH_4 consumption after 1 h of time on stream (TOS) was negligible (1.31 mmol·g_{cat}^{-1}·min^{-1}), whereas a considerably higher rate of methane consumption (20.4 mmol·g_{cat}^{-1}·min^{-1}) was recorded for Ni-MA. However, after 10 h of TOS, the activity of Ni-MA decreased significantly to 14.1 mmol·g_{cat}^{-1}·min^{-1}. Bimetallic catalysts showed a more stable rate of methane consumption (19.1 mmol·g_{cat}^{-1}·min^{-1}, after 10 h of TOF) when compared to Ni-MA, indicative of a stabilizing effect of Fe in Ni catalysts.

In order to describe the effect of Ni and Fe on the activity of the catalysts, the rates of methane consumption (after 1 h TOS) are plotted as a function of the quantity of surface Ni in the catalysts, as determined by hydrogen chemisorption (Figure 3b). The methane consumption was found to decrease with a decreasing quantity of surface Ni. For Ni-rich materials (0.75 ≤ Ni/(Ni + Fe), a linear decrease is observed, while for Fe-rich materials (0.5 ≥ Ni/(Ni + Fe), a slight deviation from linearity was noticed. In line with this observation, the rate of methane consumption normalized by the quantity of surface Ni (Figure S11a) gives a constant value for Ni-rich materials, while lower values are found for Fe-rich materials. These results indicate that CH_4 is activated on surface Ni sites, at least under the conditions studied here (650 °C). Thus, Ni is the active species for DRM, while Fe acts as a promoter in Ni-rich materials improving their stability. The exact role of Fe will be discussed in more detail further below.

To quantify the extent of the side reactions, Figure S11b plots the experimentally obtained H_2/CO ratio as a function of the rate of CO formation (after 10 h TOS). The equilibrium thermodynamic predictions considering the DRM and reverse water−gas shift (RWGS) reactions are included in Figure S11b.[12] The experimental data are in line with thermodynamic equilibrium predictions, thus, suggesting that the RWGS reaction is close to equilibrium and controlling the H_2/CO ratio. In addition, we observed that the H_2/CO ratios obtained in bimetallic systems (and in Fe-MA) are slightly lower than the thermodynamic equilibrium predictions, whereas Ni-MA shows a higher H_2/CO ratio than predicted by equilibrium thermodynamics. This is probably due to further side reactions

DOI: 10.1021/jacs.6b11487
J. Am. Chem. Soc. 2017, 139, 1937−1949

such as methane decomposition ($CH_4 \rightarrow C + 2\ H_2$) or the Boudouard reaction ($2\ CO \rightarrow C + CO_2$) occurring simultaneously; both of these side reactions were not considered in the thermodynamic calculations. Hence, using this indirect measure, a higher rate of carbon formation is expected for Ni-MA when compared to Fe-MA and the bimetallic catalysts.

3.4. Effect of Fe on Carbon Formation. Carbon deposition on the catalysts during DRM was quantified by performing TPO on the spent catalyst and reactive tests on fresh catalysts. Further structural and microstructural information concerning the carbon deposited was obtained by Raman spectroscopy and electron microscopy analyses of the spent catalysts.

Under TPO conditions, a weight loss was observed in the temperature range 150−750 °C due to the oxidation of carbonaceous species to gaseous CO_x (Figure S12). The recorded weight losses were in the following order: Ni-MA (34 wt %), Ni_4Fe_1-MA (21 wt %), and Ni_3Fe_1-MA (18 wt %), whereby the temperature required to oxidize the carbon deposited increases in the inverse order. The rate of carbon formation under DRM conditions was quantified and normalized by surface Ni (Figure S13a). In the initial stage of the reaction, the rate of carbon formation (in $\mu mol_C \cdot mol_{Surface\ Ni}^{-1} \cdot h^{-1}$) decreased in the following order: Ni-MA (0.382) > Ni_4Fe_1-MA (0.242) > Ni_3Fe_1-MA (0.230). Plotting the rate of methane consumption after 10 h TOS normalized by the initial rate of methane consumption (1 h TOS) as a function of the rate of carbon formation for the different catalysts tested (Figure 4a) revealed a linear relationship, a strong indication that catalyst deactivation is largely due to the blockage of active sites by coke.

Raman spectra of spent Ni-MA, Ni_4Fe_1-MA, and Ni_3Fe_1-MA show characteristic D and G bands of carbon (at 1250−1350 cm^{-1} and 1500−1700 cm^{-1}, respectively, Figure S13b). The D band is related to disordered carbon species (e.g., amorphous or defective filamentous carbon), whereas the G band represents the stretching mode of the sp^2 bond in ordered graphite.[72,73] The relative intensity between the D and G bands (I_D/I_G, Figure 4b) can be used to describe the degree of crystallinity of the deposited carbon, whereby the microcrystalline planar size can be calculated using Tuinstra and Koenig's law.[74] Figure 4b shows that the ratio I_D/I_G decreases from 0.94 for Ni-MA to 0.66 for Ni_3Fe_1-MA, indicative of a decreasing crystallinity of the deposited carbon with increasing Fe content in the catalyst (for Ni-rich materials). The crystallinity of the carbon deposited affects the oxidation temperature of carbon, with the oxidation temperature increasing with an increasing degree of carbon crystallinity. This is consistent with the trends observed in the TPO experiments (Figure S12).

TEM and HR-TEM images of spent Ni-MA and Ni_4Fe_1-MA illustrate visually the filamentous character of the carbon deposited on both catalysts (Figure 5). On monometallic Ni particles (Ni-MA), we observed the separation of the Ni particles from the support (Figure 5a). In agreement with TGA and Raman measurements, HR-TEM imaging shows a well-ordered atomic structure (i.e., high degree of crystallinity) for the carbon deposited on Ni-MA (Figure 5c). On the other hand, predominantly amorphous carbon features were observed on Ni_4Fe_1-MA (Figure 5d).

3.5. Catalysts Structure under DRM Conditions. *3.5.1. Combined Operando XAS-XRD Experiments.* Our catalytic experiments revealed that Ni_4Fe_1-MA exhibits a relatively high activity combined with a high stability (unlike Ni-MA). This is attributed to a lower degree of carbon formation. Thus, to identify the underlying mechanism for the lower rate of carbon formation in Fe promoted Ni, combined operando XRD-XAS experiments (Figure S14) were performed on selected catalysts (Ni_4Fe_1-MA and Ni-MA). In these experiments the off-gas was monitored by a mass spectrometer (MS) (Figure S15).

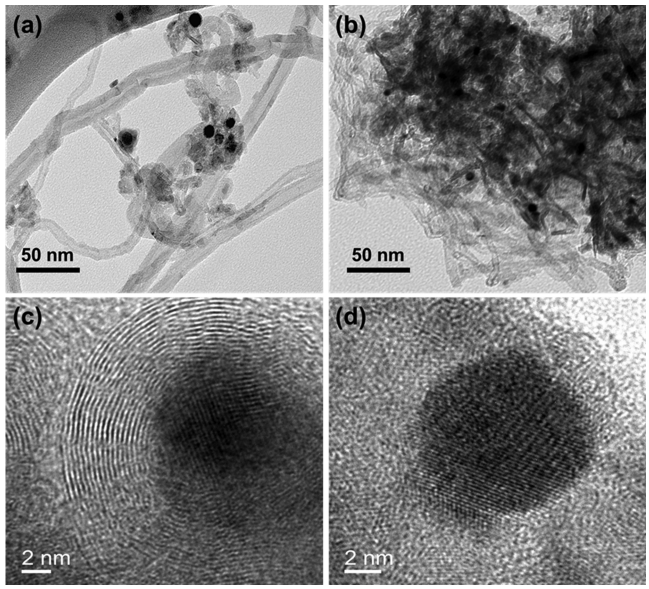

Figure 5. TEM images of (a) spent Ni-MA and (b) spent Ni_4Fe_1-MA. HR-TEM of (c) spent Ni-MA and (d) spent Ni_4Fe_1-MA.

Operando XRD data of monometallic Ni-MA (Figure S14a and Figure 6a) show that the mixture of periclase, spinel, and Ni (200) is stable under DRM conditions. We could not observe crystallite growth of any of the phases. After 2 h TOS, crystalline graphite was detected (broad peak at 2θ = 8.4°, d = 3.45 Å). The intensity of the graphite peak increased with TOS, indicative of a rapidly increasing quantity of deposited carbon. This is in agreement with TGA and Raman measurements (section 3.4). The corresponding Ni K-edge XANES spectra remained unchanged during the DRM (Figure 6c), i.e., we did not observe any oxidation of Ni. This supports further the hypothesis that the catalyst deactivation is due to carbon formation and cannot be attributed to changes in the oxidation state of the active species, i.e., Ni, e.g., through the formation of NiO, Ni_3C, or $NiAl_2O_4$, nor sintering.

The operando XRD data of Ni_4Fe_1-MA (Figure 6b) reveal a shift in the peak position of the Ni-Fe (200) reflection from 2θ = 16.31° to 16.40° with TOS, while for Ni-MA, the (200) Bragg reflection remained at 2θ = 16.42° (Figure 6a). Hence, Ni_4Fe_1-MA dealloyed during DRM, leading to a Ni-richer alloy. Using Vegard's law (Figure 1), we determined an increase in the Ni/(Ni + Fe) ratio from 0.8 to 0.87 over 5 h TOS for Ni_4Fe_1-MA. Similar to Ni-MA, also the Ni XANES spectra of Ni_4Fe_1-MA did not show any appreciable changes with TOS (Figure 6c). Furthermore, the operando XRD data of Ni_4Fe_1-MA (Figure S14b) did not reveal any changes in the structure of the support nor of the active phase with TOS. On the other hand, operando Fe XANES of Ni_4Fe_1-MA (Figure 6d, corresponding LCF analysis in Figure S14c) shows that Fe is oxidized partially to FeO under DRM conditions, viz. after 5 h TOS, 40% of the Fe in the material was in the oxidation state

DOI: 10.1021/jacs.6b11487
J. Am. Chem. Soc. 2017, 139, 1937−1949

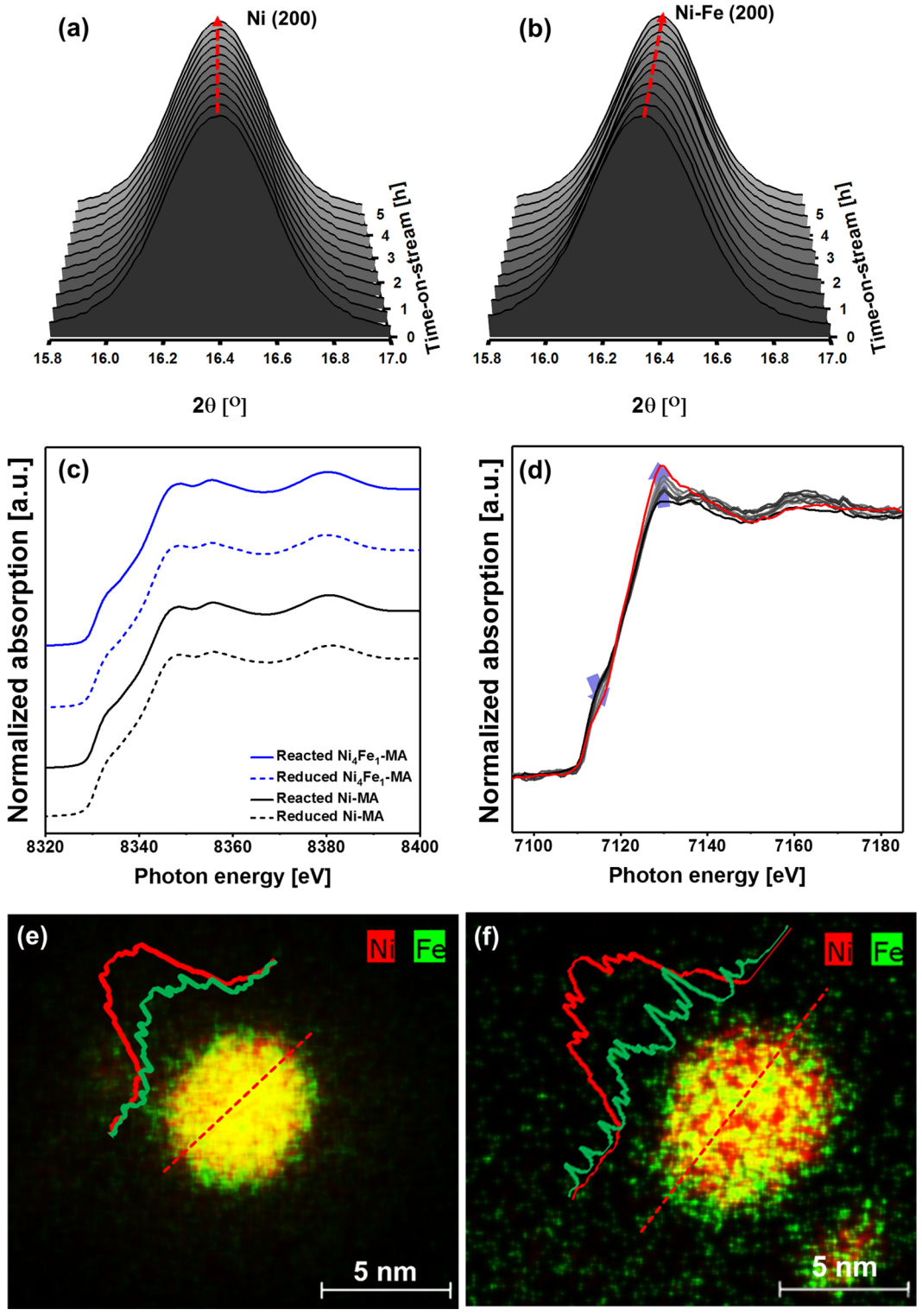

Figure 6. Ni (200) and Ni-Fe (200) regions of the operando XRD data of (a) Ni-MA and (b) Ni_4Fe_1-MA as a function of time on stream (λ = 0.5060 Å). (c) Selected operando XANES profiles (Ni K-edge) of reduced and reacted Ni-MA and Ni_4Fe_1-MA and (d) operando XANES of Ni_4Fe_1-MA (Fe K-edge) under DRM. STEM EDX of (e) reduced and (f) reacted Ni_4Fe_1-MA.

2+, leading in turn to a more Ni-rich (remaining) alloy as observed by XRD.

EXAFS analysis (Tables S1 and S2, Figures S16 and S17) of the reacted catalysts (acquired in the *in situ* setup after cooling down to 50 °C in He) confirms these observations and provides further structural insight. As shown in Figures S16b and S16d, the FT EXAFS functions at the Ni edge of Ni-MA and Ni_4Fe_1-MA did not change considerably with TOS, implying that the local order around Ni atoms was similar before and after reaction. On the other hand, the local order around Fe changed significantly with TOS. We observe a marked reduction of the amplitude of the first Fe-metal coordination sphere in the reacted material when compared to the sample prior to reaction. In addition, EXAFS fittings of the

DOI: 10.1021/jacs.6b11487
J. Am. Chem. Soc. 2017, 139, 1937−1949

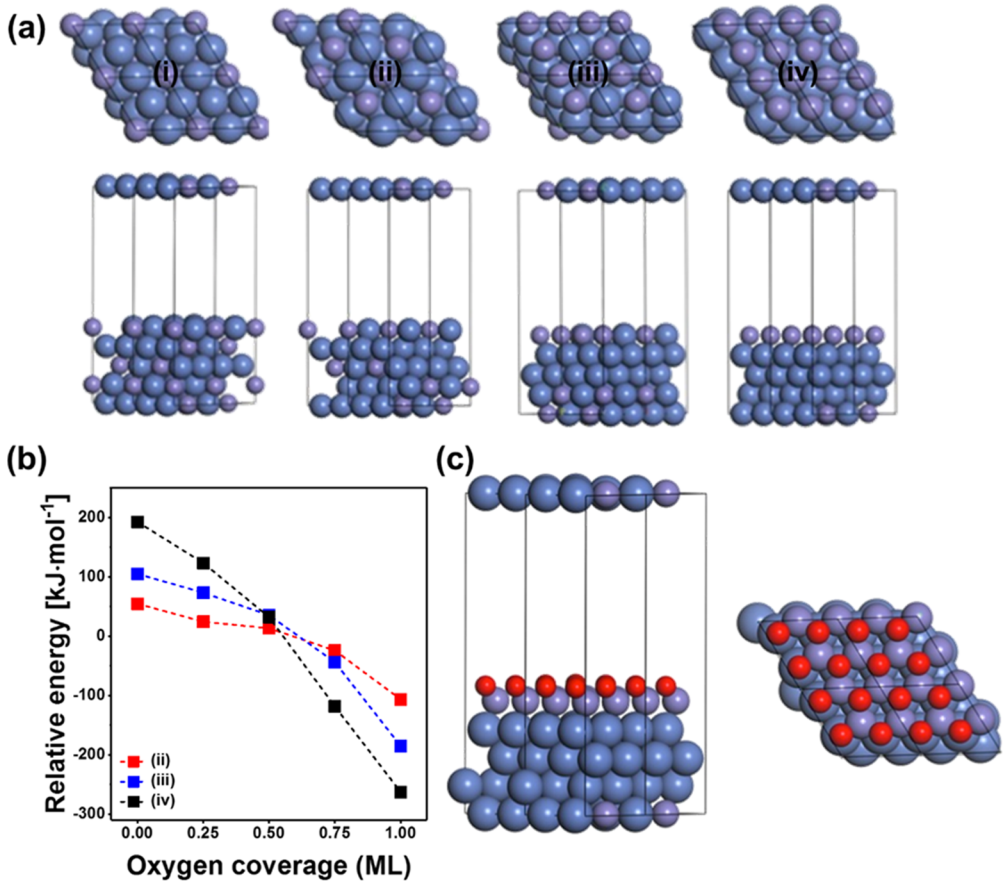

Figure 7. (a) Slabs used to model Fe migration to the surface (i–iv) and (b) the relative energy ($E_{ii-iv} - E_i$) as a function of O* coverage. (c) Detailed structure of the FeO-like (111) monolayer on Ni (111) after Fe migration to the top layer.

bimetallic Ni_4Fe_1-MA after reaction showed the presence of a Fe-O shell (Tables S1 and S2), implying that Fe is present in both metallic and oxide environments. We also observe that in the reacted sample, the total Fe-metal coordination number is considerably smaller compared to the Ni-metal coordination number, indicative for the migration of Fe to the surface. The best fit at the Fe edge is achieved by considering the presence of a Fe-O (1.98 ± 0.02 Å) and an additional first Fe-Fe shell (at 3.1 ± 0.02 Å). This Fe-Fe interatomic distance is similar to the Fe-Fe interatomic distance in FeO (3.07 Å according to crystallographic information). Moreover, the absence of Bragg reflections corresponding to bulk iron oxides in the XRD patterns rules out that iron oxide exists as a separate phase and indicates that the formed oxide is present in small domains. A further confirmation of the migration of Fe and dealloying can be obtained by comparing the partial coordination numbers at the Ni edge. During reaction, the Ni-Ni coordination number increases from 7.7 ± 0.7 (before reaction) to 9.6 7.7 ± 0.8 (after reaction), while the Ni-Fe coordination number decreases (from 1.4 ± 0.7 to 0.9 ± 0.8). The increase of homometallic (Ni-Ni) coordination at the cost of heterometallic coordination implies that after reaction, Ni has a Ni-richer environment, which would be in line with dealloying.

Thus, by combining *in situ* XAS and XRD results, we can conclude that during DRM, Fe migrates to the surface and is oxidized partially to FeO, resulting in the partial dealloying of the catalyst particles and the formation of a Ni-richer (remaining) alloy. Moreover, the combined XAS-XRD analysis indicates that the iron oxide formed during the DRM is present in small domains on the surface of the catalyst particles (i.e., on the surface of a Ni-rich alloy). Further insight in this aspect is obtained by the following STEM-EDX analysis of the reduced and spent catalysts.

3.5.2. Ni and Fe Distribution by STEM-EDX Mapping. STEM-based EDX mapping of Ni_4Fe_1-MA after reduction in H_2 (Figure 6e) shows that Fe is distributed homogeneously in the bimetallic particles. After 10 h TOS (Figure 6f), Fe- and Ni-rich regions can be observed, whereby Fe is found preferentially at the surface of the nanoparticles. This observation, in combination with our operando XRD-XAS results of a partial dealloying of NiFe through the formation of small domains of FeO under DRM conditions, suggests that the Fe-rich areas on the surface of the NiFe nanoparticles are likely to be composed of iron oxide.

3.6. DFT Calculations. In order to understand the origin of the improved reactivity of NiFe catalysts and the dealloying of Fe in NiFe catalysts, a Ni_3Fe_1 (111) surface was modeled by means of DFT calculations. We compared the adsorption energy values and DRM energetics on this system to the one of a monometallic Ni (111) surface. We considered a route in which the direct CO_2 activation yields CO* and O*, the latter oxidizing CH* as the prevailing DRM mechanism. This was shown to be the preferred path for a Ni (111) surface.[75]

The adsorption energy values calculated for DRM intermediates on Ni and Ni_3Fe_1 surfaces (Table S3) are, for most of the species, independent of Ni alloying with Fe. Nevertheless, the presence of Fe in the alloy makes the binding of oxygen-containing species more favorable due to the stronger Fe-O

DOI: 10.1021/jacs.6b11487
J. Am. Chem. Soc. 2017, 139, 1937–1949

interaction compared to the Ni-O interaction. On the Ni_3Fe_1 surface, adsorbed O* and HCO* species bind preferentially to the fcc site close to the Fe atom. The increase in the adsorption strength of the O* and HCO* species when compared to the pure Ni surface is equal to 25 and 11 kJ mol^{-1}, respectively (entries 6 and 7 of Table S2). Another difference between Ni (111) and Ni_3Fe_1 (111) surfaces is the slightly lower binding strength of the C* atom (by ca. 10 kJ mol^{-1}) for the alloy (Table S3, entry 7).

The energetics (reaction energy and energy barrier values) of the elementary steps of the DRM reaction are shown in Table S4, whereas Figure S18 plots the reaction energy diagram for DRM on Ni and Ni_3Fe_1 (111) surfaces. The key steps controlling the steady-state concentrations of O* and C* as well as the activity of the catalyst are the activation of C-O and C-H bonds from CO_2 and CH_4, respectively.[75] According to experimental work for Ni-based catalysts and theoretical calculations on the Ni (111) surface, the dissociation of CH_4 is believed to be the rate-determining step.[75,76] CH_4 activation has similar energetics for Ni and Ni_3Fe_1 (111) surfaces, although the energy barrier is slightly higher for the latter. The energy barriers for the first step of C−H activation are 82 and 91 kJ mol^{-1} for Ni and Ni_3Fe_1, respectively (Table S4, entry 1). In addition, for most of the elementary steps involving C−H bond cleavage (entries 2−4 of Table S4) and HCO* species (entries 6−7 of Table S4), similar energetics are found for Ni and Ni_3Fe_1 surfaces. However, on the Ni_3Fe surface, the activation energy for CO_2 splitting is almost 30 kJ mol^{-1} lower compared to pure Ni, i.e., 31 versus 58 kJ mol^{-1} (Table S4, entry 5). Hence, CO_2 is activated more easily on the model Ni_3Fe_1 surface. An enhanced activation of CO_2 on Ni_3Fe_1 (while possessing a comparable CH_4 activation activity as Ni) yields a larger quantity of O* species available on a Ni_3Fe_1 surface, which in turn would explain the reduced extent of carbon deposition on NiFe surfaces due to the oxidation of CH_x species by O*.

Moreover, the higher availability of adsorbed O* on Ni_3Fe_1 (111) compared to a Ni (111) surface may induce changes in the alloy structure. Thus, we have evaluated the thermodynamics of Fe migration from the bulk to the surface of the alloy with increasing O* coverages (Figure 7a,b). The migration of iron was modeled using a set of Ni_3Fe_1 (111) surfaces (Figure 7a, i−iv) in which the Ni atoms in the upmost layer were exchanged successively with Fe atoms from the layers below. The energies of such slabs exposing either clean or oxygen-covered surfaces upon different O* coverages were compared. Figure 7b shows that for the cases where little or no oxygen is adsorbed on the surface (0 to 0.5 monolayer, ML, coverage), the three Fe-enriched surfaces (ii−iv) are less stable than the original "homogeneous" alloy (i). However, for O* coverages of 0.75 and 1.0 ML, the trend is reversed, and the surfaces that expose an increased number of Fe atoms are preferred thermodynamically. For instance, for a surface coverage of 1.0 ML O*, surface "iv" is 260 kJ mol^{-1} more stable than the original Ni_3Fe_1 (111) surface "i". Hence, we can conclude that owing to the higher binding energy of oxygen to Fe than to Ni, segregation and the migration of Fe to the top of the surface are thermodynamically preferred. Indeed, for a surface coverage of 1.0 ML O* (Figure 7c), the energetically most preferred surface has a Fe to O ratio of 1:1 and is very similar to the FeO (111) monolayers that have been reported previously (experimentally and theoretically) on Pd and Pt (111) surfaces.[77]

To summarize, our DFT calculations show that the migration of Fe to the surface and the formation of a FeO layer on the surface of a Ni_3Fe_1 alloy are favored thermodynamically. This theoretical observation is in good agreement with our STEM and operando XAS and XRD measurements that also point to a partial dealloying of Ni-Fe and the formation of FeO under DRM conditions. In addition, DFT indicates that on Ni_3Fe_1, there is a larger availability of atomic oxygen due to an enhanced CO_2 activation when compared to a monometallic Ni surface.

3.7. Fe and Ni Spatial Distribution on Model Alloy Thin Films. To monitor and understand the migration and oxidation of Fe in a NiFe alloy under DRM conditions (as indicated by DFT and *in situ* XAS and XRD) in more detail, thin films composed of a NiFe alloy were prepared by cosputtering (Figure 8a). Homogeneous NiFe films with a Ni:Fe ratio of 4:1 were obtained after sputtering (Figure S19). EDX mapping of the reduced films (H_2 at 850 °C) confirmed the formation of a NiFe alloy (Figure 8a). Probing FIB cuts of the film by EDX mapping (after reduction and exposure to DRM conditions) allowed us to visualize in detail whether Fe migrates to the surface during the DRM and whether Fe is oxidized preferentially. Figure 8b shows that under DRM conditions Fe diffuses outward, i.e., to the surface of the film, resulting in dealloying. Elemental mapping of oxygen, Fe, and Ni indicates clearly the formation of a FeO_x layer on the film surface, whereas Ni remains at oxidation state Ni^0. These results are in full agreement with operando XRD and XAS studies and DFT modeling.

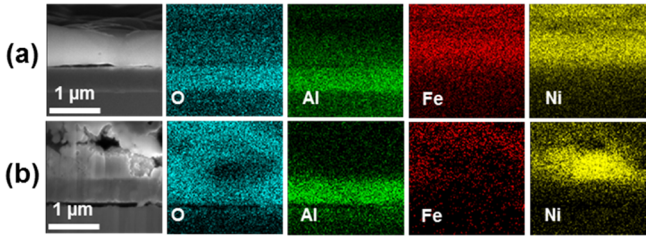

Figure 8. SEM images showing FIB cross sections of a Ni_4Fe_1 thin film sputtered onto a Al_2O_3-coated Si substrate along with EDX mapping, O (cyan), Al (green), Fe (red), and Ni (yellow): (a) after reduction in H_2 at 850 °C and (b) after exposure to DRM conditions for 5 h.

3.8. Probing the Carbon Removal Mechanism. As we have established by DFT calculations and experimentally the formation of FeO (most likely only small patches of a few atom layer thickness due to the absence of a XRD signature) under DRM conditions through the reaction of Fe and O* (CO_2 → CO + O*), we assess in the following the role of FeO in the removal of carbon under DRM conditions. To this end, the following experimental protocol was applied. After 5 h TOS (Ni_4Fe_1-MA), the reaction mixture (CH_4 + CO_2) was switched to He, while acquiring combined XAS-XRD-MS measurements for several minutes. Subsequently, the temperature was increased from 650 to 800 °C in steps of 50 °C. LCF analysis of the acquired *in situ* XANES data (Figure 9a and S20) showed that in a He atmosphere FeO was reduced partially to Fe at 650 °C. Increasing the temperature further resulted in an increasing rate and degree of the reduction of FeO. At the end of the experiment (800 °C), FeO was reduced completely to Fe^0. Simultaneous with the reduction of FeO, the production of CO was detected by mass spectrometry (Figure 9b). Thus, FeO

DOI: 10.1021/jacs.6b11487
J. Am. Chem. Soc. 2017, 139, 1937−1949

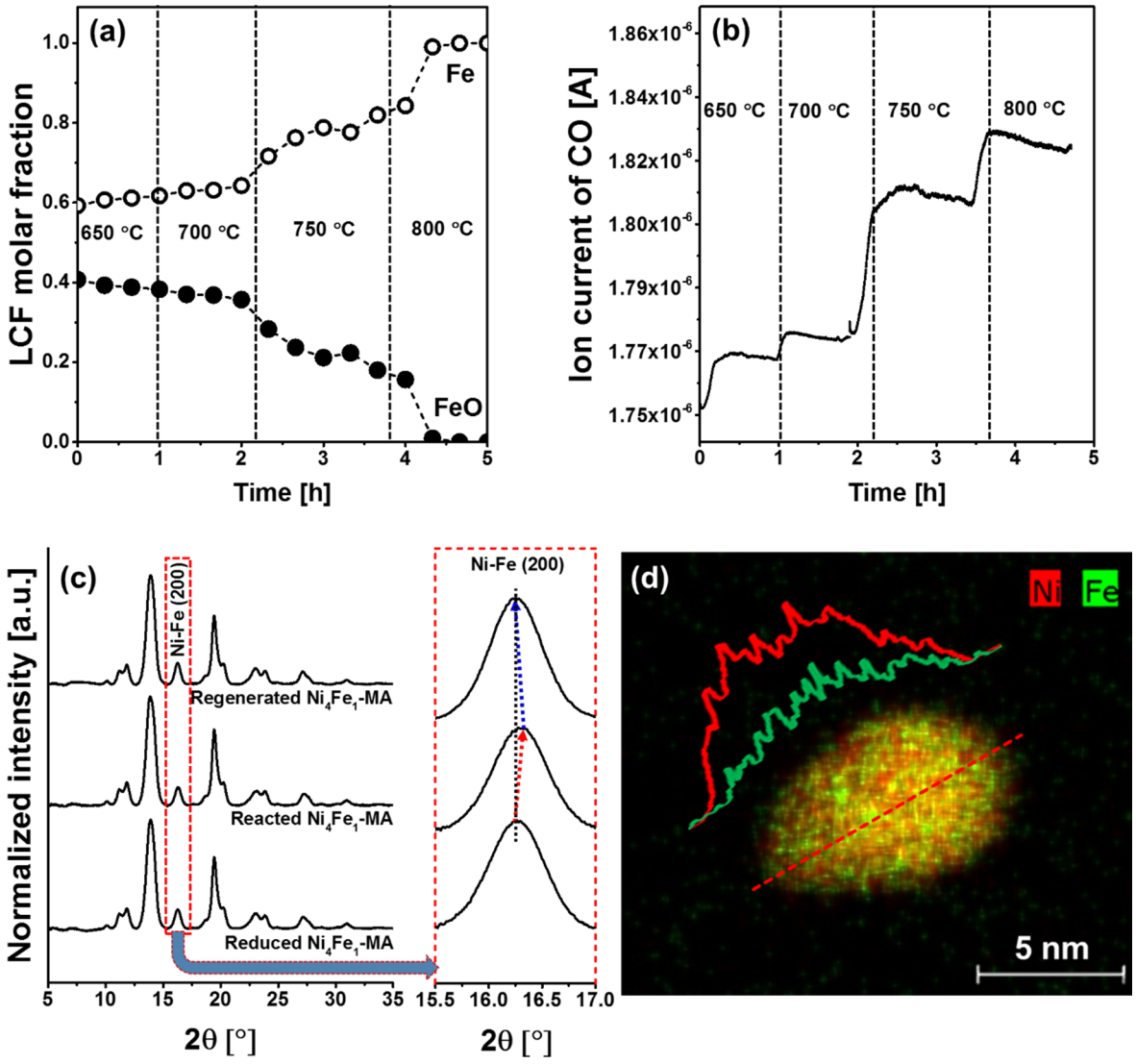

Figure 9. (a) LCF analysis of Fe K-edge XANES data and (b) the simultaneously acquired CO MS signal, collected on Ni_4Fe_1-MA, under a He atmosphere after 5 h of TOS, at the temperatures indicated in the plots. (c) XRD data collected during the same experiment at 650 °C, after reduction (reduced Ni_4Fe_1-MA), after 5 h of DRM (reacted Ni_4Fe_1-MA), and after treatment at 800 °C in an inert (He) atmosphere (regenerated Ni_4Fe_1-MA). (d) STEM EDX mapping of regenerated Ni_4Fe_1-MA in an inert (He) atmosphere.

provides lattice oxygen (O*) to surface carbon, oxidizing it partially to CO (O* + C* → CO). Simultaneously acquired XRD data (Figure 9c) confirmed that after exposing the reacted catalyst at 800 °C to a He atmosphere, realloying occurred. This was evidenced by a shift of the Ni-Fe (200) peak position to lower angles when compared to the reacted material (data were collected at the same temperature).

These measurements allow us to propose that the small domains of FeO located at the surface of the NiFe nanoparticles are in close proximity to active surface Ni, yielding catalysts with an improved coke resistance (via a FeO redox cycle, Fe + O* ↔ FeO) and hence activity. The following competitive carbon formation and carbon removal reactions are expected to occur under DRM conditions:[43]

$$CH_4 \rightarrow 2H_2 + C \quad (1)$$

$$CO_2 + Fe \rightarrow CO + FeO \quad (2)$$

$$C + FeO \rightarrow CO + Fe \quad (3)$$

STEM-EDX mapping of the material after regeneration in He reveals a homogeneous distribution of Ni and Fe in the particle (Figure 9d), confirming the realloying of Ni and Fe (as determined also by *in situ* XRD) through the reduction of FeO and simultaneous oxidation of the deposited carbon. These results demonstrate that the material can recover its original structure after carbon removal and underline the dynamic nature of the material, which undergoes dealloying through oxidation by CO_2 and realloying through its reduction by carbon species. Our results differ appreciably from previous reports that showed substantial phase separation in the catalysts under atmospheres with a high H_2/CO_2 ratio.[77]

4. CONCLUSIONS

Bimetallic Ni-Fe DRM catalysts supported on $Mg_xAl_yO_z$ with very similar morphological parameters show an increasing activity and stability, with a maximum at a Ni/(Ni + Fe) ratio of 0.8. Operando X-ray synchrotron-based studies complemented by *ex situ* characterization techniques and DFT calculations allowed us to draw the following conclusions. Under DRM

DOI: 10.1021/jacs.6b11487
J. Am. Chem. Soc. 2017, 139, 1937−1949

conditions: (1) Ni remains at oxidation state Ni^0 independently whether it is alloyed with Fe or not; (2) the deactivation of monometallic Ni is due to the formation of graphitic coke and whiskers; (3) while Fe is inactive for DRM, it improves the stability of Ni-based catalysts and the optimal catalyst composition is Ni_4Fe_1; (4) Fe in NiFe alloys is partially oxidized to FeO, leading to a partial dealloying and the formation of a Ni-richer Ni-Fe alloy; (5) FeO is located preferentially at the surface as small domains of a few atom layer thickness covering a fraction of the Ni-rich particles; and (6) the thus-formed FeO reacts with carbon deposits, leading in turn to a reduced coke formation. These findings explain the increased catalytic stability of bimetallic NiFe catalysts via a $Fe^{2+}O/Fe^0$ redox cycle. The presence and migration of FeO toward the surface, which allows its reaction with carbon deposits, are essential features of these catalysts, and it illustrates how important dynamic phenomena are, even for such supported bimetallic nanoparticle catalysts.

■ ASSOCIATED CONTENT

Supporting Information

The Supporting Information is available free of charge on the ACS Publications website at DOI: 10.1021/jacs.6b11487.

Details and characterization of materials by N_2 physisorption, TEM, H_2 TPR, TGA, Raman, EDS measurements. Description of the operando XRD/XAS setup, operando XRD/XANES/EXAFS analysis and DFT calculations (PDF)

■ AUTHOR INFORMATION

Corresponding Author

*muelchri@ethz.ch

ORCID

Aleix Comas-Vives: 0000-0002-7002-1582

Christophe Copéret: 0000-0001-9660-3890

Notes

The authors declare no competing financial interest.

■ ACKNOWLEDGMENTS

C.C. and C.M. gratefully acknowledge support from the ETH Research grant (ETH 57 12-2). C.C. also thanks SCCER Heat and Energy Storage for cofunding this project, and C.M. acknowledges the Swiss National Science Foundation (206021_144986). L.F. and A.C.-V. acknowledge financial support from the ETH Research grant (ETH42 14-1) and the Ambizione Fellowship (PZ00P2_148059), respectively. We would like to thank Lydia Zehnder for her support with XRD measurements and the Scientific Center for Optic and Electron Microscopy (ScopeM) for providing access to electron microscopes. ESRF and the Swiss Norwegian Beamlines (SNBL at ESRF) are acknowledged gratefully for providing access to the synchrotron facility. We thank Dr. Olga Safonova for helpful discussions concerning EXAFS analysis.

■ REFERENCES

(1) Bitter, J. H.; Seshan, K.; Lercher, J. A. *J. Catal.* **1997**, *171*, 279.
(2) Bradford, M. C. J.; Vannice, M. A. *J. Catal.* **1999**, *183*, 69.
(3) Erdohelyi, A.; Cserenyi, J.; Solymosi, F. *J. Catal.* **1993**, *141*, 287.
(4) Fan, M.-S.; Abdullah, A. Z.; Bhatia, S. *ChemCatChem* **2009**, *1*, 192.
(5) Li, D.; Nakagawa, Y.; Tomishige, K. *Appl. Catal., A* **2011**, *408*, 1.
(6) Rostrupnielsen, J. R.; Hansen, J. H. B. *J. Catal.* **1993**, *144*, 38.
(7) Trimm, D. L. *Catal. Today* **1999**, *49*, 3.
(8) Van Dillen, A. J.; Terörde, R. J.; Lensveld, D. J.; Geus, J. W.; De Jong, K. P. *J. Catal.* **2003**, *216*, 257.
(9) Xu, L.; Song, H.; Chou, L. *ACS Catal.* **2012**, *2*, 1331.
(10) Kim, J.-H.; Suh, D. J.; Park, T.-J.; Kim, K.-L. *Appl. Catal., A* **2000**, *197*, 191.
(11) Frusteri, F.; Spadaro, L.; Arena, F.; Chuvilin, A. *Carbon* **2002**, *40*, 1063.
(12) Baudouin, D.; Rodemerck, U.; Krumeich, F.; Mallmann, A. d.; Szeto, K. C.; Ménard, H.; Veyre, L.; Candy, J.-P.; Webb, P. B.; Thieuleux, C.; Copéret, C. *J. Catal.* **2013**, *297*, 27.
(13) Djaidja, A.; Libs, S.; Kiennemann, A.; Barama, A. *Catal. Today* **2006**, *113*, 194.
(14) Horváth, A.; Stefler, G.; Geszti, O.; Kienneman, A.; Pietraszek, A.; Guczi, L. *Catal. Today* **2011**, *169*, 102.
(15) Daza, C. E.; Cabrera, C. R.; Moreno, S.; Molina, R. *Appl. Catal., A* **2010**, *378*, 125.
(16) Eltejaei, H.; Reza Bozorgzadeh, H.; Towfighi, J.; Reza Omidkhah, M.; Rezaei, M.; Zanganeh, R.; Zamaniyan, A.; Zarrin Ghalam, A. *Int. J. Hydrogen Energy* **2012**, *37*, 4107.
(17) Mondal, K. C.; Choudhary, V. R.; Joshi, U. A. *Appl. Catal., A* **2007**, *316*, 47.
(18) Therdthianwong, S.; Siangchin, C.; Therdthianwong, A. *Fuel Process. Technol.* **2008**, *89*, 160.
(19) Chen, Y.-g.; Yamazaki, O.; Tomishige, K.; Fujimoto, K. *Catal. Lett.* **1996**, *39*, 91.
(20) Chen, Y.-g.; Tomishige, K.; Yokoyama, K.; Fujimoto, K. *Appl. Catal., A* **1997**, *165*, 335.
(21) Crisafulli, C.; Scirè, S.; Maggiore, R.; Minicò, S.; Galvagno, S. *Catal. Lett.* **1999**, *59*, 21.
(22) Hou, Z.; Yashima, T. *Catal. Lett.* **2003**, *89*, 193.
(23) Pawelec, B.; Damyanova, S.; Arishtirova, K.; Fierro, J. L. G.; Petrov, L. *Appl. Catal., A* **2007**, *323*, 188.
(24) Steinhauer, B.; Kasireddy, M. R.; Radnik, J.; Martin, A. *Appl. Catal., A* **2009**, *366*, 333.
(25) Rahemi, N.; Haghighi, M.; Babaluo, A. A.; Jafari, M. F.; Khorram, S. *Int. J. Hydrogen Energy* **2013**, *38*, 16048.
(26) Zhang, J.; Wang, H.; Dalai, A. K. *J. Catal.* **2007**, *249*, 300.
(27) Djinović, P.; Osojnik Črnivec, I. G.; Erjavec, B.; Pintar, A. *Appl. Catal., B* **2012**, *125*, 259.
(28) Bonura, G.; Cannilla, C.; Frusteri, F. *Appl. Catal., B* **2012**, *121−122*, 135.
(29) Nikolla, E.; Holewinski, A.; Schwank, J.; Linic, S. *J. Am. Chem. Soc.* **2006**, *128*, 11354.
(30) Guo, X.; Fang, G.; Li, G.; Ma, H.; Fan, H.; Yu, L.; Ma, C.; Wu, X.; Deng, D.; Wei, M.; Tan, D.; Si, R.; Zhang, S.; Li, J.; Sun, L.; Tang, Z.; Pan, X.; Bao, X. *Science* **2014**, *344*, 616.
(31) Chen, M.; Kumar, D.; Yi, C.-W.; Goodman, D. W. *Science* **2005**, *310*, 291.
(32) Kyriakou, G.; Boucher, M. B.; Jewell, A. D.; Lewis, E. A.; Lawton, T. J.; Baber, A. E.; Tierney, H. L.; Flytzani-Stephanopoulos, M.; Sykes, E. C. H. *Science* **2012**, *335*, 1209.
(33) Ding, Y.; Fan, F.; Tian, Z.; Wang, Z. L. *J. Am. Chem. Soc.* **2010**, *132*, 12480.
(34) Morales, F.; Weckhuysen, B. M. In *Catalysis*; Spivey, J. J., Dooley, K. M., Eds.; The Royal Society of Chemistry: Cambridge, 2006; Vol. *19*.
(35) Andersson, M. P.; Bligaard, T.; Kustov, A.; Larsen, K. E.; Greeley, J.; Johannessen, T.; Christensen, C. H.; Nørskov, J. K. *J. Catal.* **2006**, *239*, 501.
(36) Ober, J. A.; *Mineral commodity summaries 2016*; U.S. Geological Survey: Reston, VA, 2016; p 205.
(37) Koike, M.; Li, D.; Nakagawa, Y.; Tomishige, K. *ChemSusChem* **2012**, *5*, 2312.
(38) Wang, L.; Chen, J.; Watanabe, H.; Xu, Y.; Tamura, M.; Nakagawa, Y.; Tomishige, K. *Appl. Catal., B* **2014**, *160−161*, 701.
(39) Wang, L.; Li, D.; Koike, M.; Koso, S.; Nakagawa, Y.; Xu, Y.; Tomishige, K. *Appl. Catal., A* **2011**, *392*, 248.

DOI: 10.1021/jacs.6b11487
J. Am. Chem. Soc. 2017, 139, 1937−1949

(40) Baudouin, D.; Margossian, T.; Rodemerck, U.; Webb, P. B.; Veyre, L.; Krumeich, F.; Candy, J.-P.; Thieuleux, C.; Copéret, C. *ChemCatChem* (accepted), http://dx.doi.org/10.1002/cctc.201600582.
(41) Tsoukalou, A.; Imtiaz, Q.; Kim, S. M.; Abdala, P. M.; Yoon, S.; Müller, C. R. *J. Catal.* **2016**, *343*, 208.
(42) Koike, M.; Li, D.; Watanabe, H.; Nakagawa, Y.; Tomishige, K. *Appl. Catal., A* **2015**, *506*, 151.
(43) Theofanidis, S. A.; Galvita, V. V.; Poelman, H.; Marin, G. B. *ACS Catal.* **2015**, *5*, 3028.
(44) Theofanidis, S. A.; Batchu, R.; Galvita, V. V.; Poelman, H.; Marin, G. B. *Appl. Catal., B* **2016**, *185*, 42.
(45) Benrabaa, R.; Boukhlouf, H.; Löfberg, A.; Rubbens, A.; Vannier, R.-N.; Bordes-Richard, E.; Barama, A. *J. Nat. Gas Chem.* **2012**, *21*, 595.
(46) Mette, K.; Kühl, S.; Düdder, H.; Kähler, K.; Tarasov, A.; Muhler, M.; Behrens, M. *ChemCatChem* **2014**, *6*, 100.
(47) Li, D.; Koike, M.; Wang, L.; Nakagawa, Y.; Xu, Y.; Tomishige, K. *ChemSusChem* **2014**, *7*, 510.
(48) Brunauer, S.; Emmett, P. H.; Teller, E. *J. Am. Chem. Soc.* **1938**, *60*, 309.
(49) Barrett, E. P.; Joyner, L. G.; Halenda, P. P. *J. Am. Chem. Soc.* **1951**, *73*, 373.
(50) Bartholomew, C. H.; Pannell, R. B.; Butler, J. L. *J. Catal.* **1980**, *65*, 335.
(51) Kammler, T.; Wehner, S.; Küppers, J. *Surf. Sci.* **1995**, *339*, 125.
(52) Bartholomew, C. *Catal. Lett.* **1990**, *7*, 27.
(53) Abdala, P. M.; Mauroy, H.; van Beek, W. *J. Appl. Crystallogr.* **2014**, *47*, 449.
(54) van Beek, W.; Safonova, O. V.; Wiker, G.; Emerich, H. *Phase Transitions* **2011**, *84*, 726.
(55) Lu, J.; Wei, X.; Chang, Y.; Tian, S.; Xiong, Y. *J. Chem. Technol. Biotechnol.* **2016**, *91*, 985.
(56) Yin, Y.; Zhang, B.; Zhang, X.; Xu, J.; Yang, S. *J. Sol-Gel Sci. Technol.* **2013**, *66*, 540.
(57) Ravel, B.; Newville, M. *J. Synchrotron Radiat.* **2005**, *12*, 537.
(58) Kresse, G.; Furthmüller, J. *Comput. Mater. Sci.* **1996**, *6*, 15.
(59) Kresse, G.; Hafner, J. *Phys. Rev. B: Condens. Matter Mater. Phys.* **1993**, *47*, 558.
(60) Kresse, G.; Hafner, J. *Phys. Rev. B: Condens. Matter Mater. Phys.* **1994**, *49*, 14251.
(61) Blöchl, P. E. *Phys. Rev. B: Condens. Matter Mater. Phys.* **1994**, *50*, 17953.
(62) Perdew, J. P.; Chevary, J. A.; Vosko, S. H.; Jackson, K. A.; Pederson, M. R.; Singh, D. J.; Fiolhais, C. *Phys. Rev. B: Condens. Matter Mater. Phys.* **1992**, *46*, 6671.
(63) Monkhorst, H. J.; Pack, J. D. *Phys. Rev. B* **1976**, *13*, 5188.
(64) Henkelman, G.; Uberuaga, B. P.; Jónsson, H. *J. Chem. Phys.* **2000**, *113*, 9901.
(65) Denton, A. R.; Ashcroft, N. W. *Phys. Rev. A: At., Mol., Opt. Phys.* **1991**, *43*, 3161.
(66) Vegard, L. *Eur. Phys. J. A* **1921**, *5*, 17.
(67) Greeley, J.; Mavrikakis, M. *J. Phys. Chem. B* **2005**, *109*, 3460.
(68) Tanaka, H.; Kaino, R.; Okumura, K.; Kizuka, T.; Nakagawa, Y.; Tomishige, K. *Appl. Catal., A* **2010**, *378*, 175.
(69) Zieliński, J.; Zglinicka, I.; Znak, L.; Kaszkur, Z. *Appl. Catal., A* **2010**, *381*, 191.
(70) Ge, X.; Li, M.; Shen, J. *J. Solid State Chem.* **2001**, *161*, 38.
(71) Frenkel, A. I. *Chem. Soc. Rev.* **2012**, *41*, 8163.
(72) Guo, J.; Lou, H.; Zheng, X. *Carbon* **2007**, *45*, 1314.
(73) Wang, P.; Tanabe, E.; Ito, K.; Jia, J.; Morioka, H.; Shishido, T.; Takehira, K. *Appl. Catal., A* **2002**, *231*, 35.
(74) Mallet-Ladeira, P.; Puech, P.; Toulouse, C.; Cazayous, M.; Ratel-Ramond, N.; Weisbecker, P.; Vignoles, G. L.; Monthioux, M. *Carbon* **2014**, *80*, 629.
(75) Foppa, L.; Silaghi, M.-C.; Larmier, K.; Comas-Vives, A. *J. Catal.* **2016**, *343*, 196.
(76) Wei, J.; Iglesia, E. *J. Catal.* **2004**, *224*, 370.
(77) Zeuthen, H.; Kudernatsch, W.; Peng, G.; Merte, L. R.; Ono, L. K.; Lammich, L.; Bai, Y.; Grabow, L. C.; Mavrikakis, M.; Wendt, S.; Besenbacher, F. *J. Phys. Chem. C* **2013**, *117*, 15155.

DOI: 10.1021/jacs.6b11487
J. Am. Chem. Soc. 2017, 139, 1937−1949